JVST A
Journal of Vacuum Science & Technology A

Sn-modified $BaTiO_3$ thin film with enhanced polarization

Cite as: J. Vac. Sci. Technol. A **41**, 022701 (2023); https://doi.org/10.1116/6.0002208
Submitted: 07 September 2022 • Accepted: 12 December 2022 • Published Online: 12 January 2023

William Nunn, Abinash Kumar, Rui Zu, et al.

JVST A
Journal of Vacuum Science & Technology A

ARTICLE

avs.scitation.org/journal/jva

Sn-modified $BaTiO_3$ thin film with enhanced polarization

Cite as: J. Vac. Sci. Technol. A **41**, 022701 (2023); doi: 10.1116/6.0002208
Submitted: 7 September 2022 · Accepted: 12 December 2022 ·
Published Online: 12 January 2023

William Nunn,[1] Abinash Kumar,[2] Rui Zu,[3] Bailey Nebgen,[3] Shukai Yu,[3] Anusha Kamath Manjeshwar,[1] Venkatraman Gopalan,[3,4] James M. LeBeau,[2] Richard D. James,[5] and Bharat Jalan[1,a)]

AFFILIATIONS

[1]Department of Chemical Engineering and Materials Science, University of Minnesota, Minneapolis, Minnesota 55455
[2]Department of Materials Science and Engineering, Massachusetts Institute of Technology, Cambridge, Massachusetts 02139
[3]Department of Materials Science and Engineering, Pennsylvania State University, University Park, Pennsylvania 16802
[4]Departments of Physics, and Engineering Science and Mechanics, Pennsylvania State University, University Park, Pennsylvania 16802
[5]Department of Aerospace Engineering and Mechanics, University of Minnesota, Minneapolis, Minnesota 55455

Note: This paper is a part of the Special Topic Collection on Thin Film Deposition for Materials Discovery.
[a)]**Author to whom correspondence should be addressed:** bjalan@umn.edu

ABSTRACT

Hybrid molecular beam epitaxy (MBE) growth of Sn-modified $BaTiO_3$ films was realized with varying domain structures and crystal symmetries across the entire composition space. Macroscopic and microscopic structures and the crystal symmetry of these thin films were determined using a combination of optical second harmonic generation (SHG) polarimetry and scanning transmission electron microscopy (STEM). SHG polarimetry revealed a variation in the global crystal symmetry of the films from tetragonal ($P4mm$) to cubic ($Pm\bar{3}m$) across the composition range, $x = 0$ to 1 in $BaTi_{1-x}Sn_xO_3$ (BTSO). STEM imaging shows that the long-range polar order observed when the Sn content is low ($x = 0.09$) transformed to a short-range polar order as the Sn content increased ($x = 0.48$). Consistent with atomic displacement measurements from STEM, the largest polarization was obtained at the lowest Sn content of $x = 0.09$ in Sn-modified $BaTiO_3$ as determined by SHG. These results agree with recent bulk ceramic reports and further identify this material system as a potential replacement for Pb-containing relaxor-based thin film devices.

I. INTRODUCTION

Ferroelectric materials with large polarization and a piezoelectric response have been increasingly sought after for use in a variety of devices such as capacitors and micro-electromechanical system (MEMS) devices such as sensors and actuators.[1–3] Of these, most leading ferroelectrics contain the toxic element lead as they are based on $PbTiO_3$. The most popular ferroelectric material system is lead zirconate titanate (PZT) with a large piezoelectric coefficient due, in part, to the presence of the morphotropic phase boundary.[4] Finding lead-free materials that exhibit similar properties as PZT has been given considerable attention.[5–7] Materials like, and modified based on, $BaTiO_3$, $BiFeO_3$, $Na_{0.5}Bi_{0.5}TiO_3$, and (K, Na)NbO_3 have been the focus of many studies and have shown properties similar to the lead-based ferroelectrics.[8–13]

One of these ferroelectric systems of considerable interest is the $BaTiO_3$–$BaSnO_3$ alloy system, or $BaTi_{1-x}Sn_xO_3$ (BTSO), obtained by substituting Ti with Sn at the B-site of $BaTiO_3$. Reports in bulk ceramics for the Sn incorporation of $x = 0.02$ in $BaTiO_3$ show a two-fold enhancement in the room-temperature longitudinal piezoelectric coefficient (d_{33}) over $BaTiO_3$ due to coexisting tetragonal and orthorhombic phases.[14–16] For $x = 0.11$, the presence of a quasiquadruple point, which is a state of four-phase coexistence, at a temperature of ~40 °C produced a six-fold increase in the dielectric constant at the Curie temperature and a five-fold increase in d_{33} over these corresponding properties of undoped $BaTiO_3$.[14] The phase coexistence at the quasiquadruple point creates a double morphotropic phase boundary and is thought to enhance these dielectric and

piezoelectric properties by allowing for increased polarization rotation and extension.[14]

Although most studies on BTSO use bulk ceramics, thin film growth by sol-gel methods,[17,18] sputtering,[19–22] and pulsed laser deposition (PLD)[23,24] has also been reported. Here, we report, for the first time, the molecular beam epitaxy (MBE) growth of the complete solid-solution of BTSO, from $BaTiO_3$ (BTO, $x = 0$) to $BaSnO_3$ (BSO, $x = 1$). More specifically, we use the hybrid MBE technique, which has shown its capability to grow the two end members in a high-quality manner.[25–28] Hybrid MBE substitutes the thermal evaporation or sublimation of titanium and tin metal sources with the evaporation of liquid metal-organic sources. The metal-organic precursors used here are titanium(IV) tetraisopropoxide (TTIP) for Ti and hexamethylditin (HMDT) for Sn, which are co-deposited with the thermal evaporation of Ba and an oxygen plasma source to form BTSO films. Using this approach, both $BaTiO_3$ and $BaSnO_3$ have been grown with an adsorption-controlled growth window for self-regulating stoichiometry control. Details on the growth method can be found elsewhere.[26,27]

II. RESULTS AND DISCUSSIONS

BTSO films were grown on $SrTiO_3$ (001) (STO) substrates at 950 °C, measured by a thermocouple, by varying the B-site flux ratio of TTIP to HMDT while holding the A-site flux of the elemental metal Ba constant. Individual fluxes were measured prior to growth as a beam equivalent pressure (BEP). Since the individual B-site fluxes required for BTO and BSO growth were not the same, $BEP(TTIP) = 1.1 \times 10^{-6}$ Torr and $BEP(HMDT) = 2.7 \times 10^{-6}$ Torr, respectively, fluxes were increased or decreased as a percentage of their individual total. At the end, the desired amount of Sn incorporation at the B-site was estimated using the following equation:

$$x\,(\text{BEP ratio}) = \frac{\text{BEP(HMDT)}}{\text{BEP(HMDT)} + \text{BEP(TTIP)}}. \quad (1)$$

High-resolution x-ray diffraction (HRXRD) scans around the (002) film and substrate peaks for ~40 nm films grown from $x = 0$ to $x = 1$ (bottom to top) are shown in Fig. 1(a). The c-axis of BTO, the expected out-of-plane orientation, has a smaller lattice parameter (4.036 Å) compared to the cubic lattice parameter of BSO (4.116 Å). As a result of this difference, a shift in the (002) film peak from higher to lower 2θ occurred as the HMDT flux was increased and the TTIP flux was decreased. The peak shift to lower 2θ, i.e., lattice expansion, signified not only the incorporation of Sn but also that Sn is likely substituting Ti on the B-site. At the B-site, Sn^{4+} has a larger ionic radius than Ti^{4+}, leading to the expansion of the lattice. If Sn were to go into the A-site, Sn^{2+} would have a smaller ionic radius than Ba^{2+}, indicating the opposite.

Since Sn was likely incorporated as Sn^{4+} at the B-site from HRXRD, we estimated the cationic ratios near the film surface from the peak area ratios of Ti^{4+} 2p, Sn^{4+} 3d, and Ba^{2+} 3d peaks in x-ray photoelectron spectroscopy (XPS). The peak areas in this ratio were each normalized by their corresponding atomic sensitivity factors (1.436 for Ti 2p, 5.030 for Sn 3d, and 6.038 for Ba 3d). The percentage of Sn incorporation near the surface (~5–7 nm), x (XPS), was then calculated from the following equation:

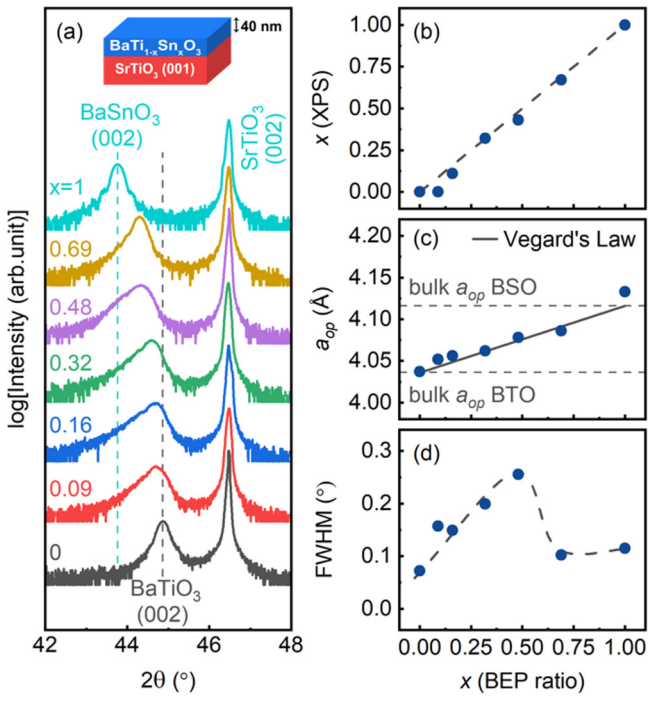

FIG. 1. (a) High-resolution x-ray diffraction patterns of ~40 nm $BaTi_{1-x}Sn_xO_3$ films on $SrTiO_3$ (001). Composition is given by the BEP ratio relation from Eq. (1). (b) Atomic percentage of Sn(x) determined by XPS plotted against its atomic percentage estimated from the BEP ratio. (c) Out-of-plane lattice parameter (a_{op}) and (d) FWHM of the film (002) rocking curve. Solid line in (c) is the expected a_{op} from Vegard's law. Dashed lines in panels (b) and (d) are guide to the eye.

$$x(\text{XPS}) = \frac{A_{Sn^{4+}3d}}{A_{Ti^{4+}3p} + A_{Sn^{4+}3d}}, \quad (2)$$

where A_x is the normalized peak area of x (either Ti^{4+} 2p or Sn^{4+} 3d). The details of the XPS measurement are similar to the study of surface termination in hybrid MBE grown $SrTiO_3$ outlined in Ref. 29.

We found a close to one-to-one relationship between x (XPS) from Eq. (2) and x (BEP ratio) from Eq. (1) as shown in Fig. 1(b). This observation suggests that the amount of Sn incorporated in $BaTiO_3$ can be reliably predicted from the growth conditions. We note that the sample with the smallest amount of Sn ($x = 0.09$) did not show a Sn signal in XPS, despite the change in the out-of-plane lattice parameter from Sn alloying in $BaTiO_3$. This difference may arise from the combination of surface contamination and the inhomogeneous distribution of Sn through the depth of the film observed in scanning transmission electron microscopy (STEM), with a higher concentration of Sn at the film-substrate interface than the surface region probed by XPS. Carbon contamination on the film surface may further attenuate the weak Sn signal from the Sn-deficient surface region, making the Sn peak detection for this film challenging.

Taking the peak intensity position from each film, the out-of-plane lattice parameter (a_{op}) was calculated and is shown in Fig. 1(c). As Sn incorporation increased, a_{op} increased from the bulk BTO value to close to the bulk BSO value as predicted by Vegard's law, which confirms that Sn substituted Ti at the B-site[30] The larger discrepancy for the BSO ($x = 1$) film has previously been shown to be due to residual strain in the film.[27]

While a_{op} was taken from the peak intensity position, the (002) film peaks were asymmetric except when $x = 0$ or $x = 1$. The asymmetry of the peak increased with increasing Sn content up to $x = 0.48$, beyond which the peak returned to a more symmetric shape. The asymmetry indicates that there is a range of lattice parameters in these alloyed films. The same trend was also observed in the FWHM of the film (002) rocking curves, seen in Fig. 1(d). Together, these trends signify increased disorder in the film as the Sn concentration increases, up to a point where it returns to a less disordered structure with a FWHM similar to that of BSO. The disorder may signify the increasing presence of multiple phases or complicated domain structures involving polar nanoregions (PNRs) as Sn is added to the structure. This will be discussed based on optical second harmonic generation (SHG) polarimetry and STEM results.

BSO has the prototypical cubic perovskite crystal structure with the space group $Pm\bar{3}m$, but, after alloying with BTO, which is tetragonal with the space group $P4mm$, it is conceivable that a change in symmetry occurs. To verify the crystal symmetry, optical second harmonic generation polarimetry was utilized, a schematic of which is shown in Fig. 2(a), where the red and blue rays are fundamental (labeled ω) and second harmonic frequencies (labeled 2ω), respectively.[31] The SHG experiment was performed using the amplified laser with a central wavelength at 800 nm (1 kHz, 100 fs) generated by a Ti:sapphire femtosecond laser system. The incident polarization was rotated as a function of azimuthal angle φ, and the incident angle (θ) is set at 45°. The p and s polarized SHG intensity ($I_p^{2\omega}$ and $I_s^{2\omega}$) were measured while rotating the incident polarization at the fundamental wavelength (described by the azimuthal φ).

SHG relies on a second-order nonlinear optical phenomenon where a nonlinear medium combines two photons at frequency ω into one photon at 2ω frequency.[31] Mathematically, this phenomenon is expressed as $P_i^{2\omega} = \chi_{ijk}^{(2)} E_j^{\omega} E_k^{\omega}$, where $P^{2\omega}$, $\chi^{(2)}$, and E^{ω} represent nonlinear polarization, SHG susceptibility, and electric field at ω, respectively. The subscripts i, j, k denote components, and the Einstein summation convention is used. Due to the symmetry constraints, the dipolar SHG response will only be seen if the material possesses the broken inversion symmetry. We experimentally confirmed that the cubic centrosymmetric BSO sample, ($x = 1$) is SHG inactive, which is consistent with our expectation for space groups with inversion symmetry. Adding Sn to BTO, an SHG signal was seen until after the $x = 0.48$ sample, signifying a large amount of Sn can substitute Ti before the structure turns centrosymmetric.

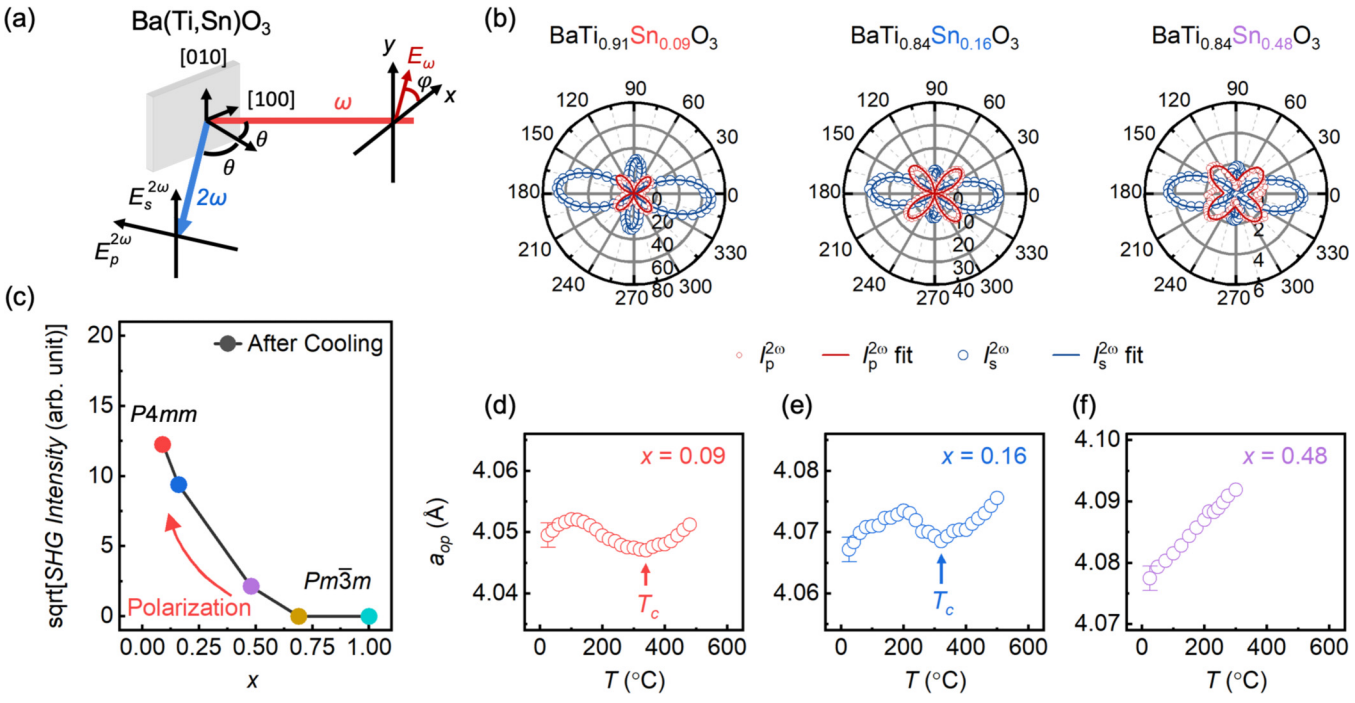

FIG. 2. (a) Schematic representation of the SHG measurement. The red and blue rays represent the fundamental (labeled ω) and second harmonic frequencies (labeled 2ω), respectively. θ is set at 45°. (b) SHG polar plots ($I_p^{2\omega}$ and $I_s^{2\omega}$) as a function of azimuthal angle φ for BTSO films. No signal was seen for $x = 1$ and 0.69. (c) Room-temperature square root of the SHG intensity, which is proportional to polarization, plotted against the Sn to Ti ratio, x, after heating to 400 °C and then cooling. (d)–(f) Temperature-dependent out-of-plane lattice parameters upon heating obtained from HRXRD. Error bars for all are the same but only displayed for the first data point.

As the amount of Sn was increased, the SHG signal decreased until it no longer could be collected at $x \geq 0.69$. Polar plots and their fittings for three Sn-modified samples which show signals are shown in Fig. 2(b). The fitting details are further discussed in supplementary material.[35] From our model, $x = 0.09$ and 0.16 can be explained by the single domain of the tetragonal phase ($P4mm$) with polarization in the out-of-plane direction, which is a promising result for enhanced ferroelectric properties of BTO. Noticeably, this result differs from bulk ceramic reports where a shift from tetragonal to orthorhombic at room temperature occurs at $x \approx 0.04$.[14] This indicates the stabilization of the higher-temperature phase in thin films, an effect most likely imparted by the substrate. As for $x = 0.48$, multidomains are considered to account for changes in the polarimetry such as broadened lobes in $I_s^{2\omega}$. The analysis suggests that multiple tetragonal domains are formed, and the major polarization direction is reoriented from the out-of-plane to the in-plane direction. Further increasing Sn leads to the loss of the SHG signal, which is consistent with a structural transition from $P4mm$ to $Pm\bar{3}m$.

SHG also allows for an estimation of the overall polarization of a material based on the collected intensity, as the square root of the SHG intensity is proportional to the polarization. By alloying from BSO to BTO, polarization shows an increase as shown in Fig. 2(c). A maximum in polarization was observed at $x = 0.09$, close to the expected maximum based on results for bulk ceramics ($x \approx 0.11$).[14] We performed SHG polarimetry on the BTO ($x = 0$) sample, but do not compare its SHG signals to the signals from Sn-modified BTO samples since STEM suggests the presence of the BaO phase in the BTO sample (Fig. S1, Ref. 35). The Sn-modified BTO samples measured similarly in STEM did not show any BaO phases.

Another important aspect of ferroelectric materials is their phase transitions. Here, a_{op} was measured as a function of temperature from HRXRD [Figs. 2(d)–2(f)]. For $x \geq 0.48$, a_{op} increases linearly with temperature [Fig. 2(f)]. However, as Sn is decreased further, a nonlinear change in a_{op} as a function of temperature occurred and resembled what is typically seen for a phase transition in these BTO-based thin films. From the local minimum at higher temperature, the T_c of 320 and 340 °C was obtained for $x = 0.16$ and 0.09, respectively. The increase in T_c with decreasing Sn does follow the usual trend of BTSO. However, we note that the actual transition temperature may be slightly different as data points were taken only every 20 °C. The change in the a_{op} of the BTO ($x = 0$) sample with increasing temperature is not included due to the presence of the BaO phase, which may affect phase transition behavior.

The peak asymmetry and the increasing FWHM from HRXRD with increasing Sn incorporation suggest that the structure, composition, and symmetry of the Sn-modified BTO films may vary microscopically. SHG can probe a large area of a sample (~20 μm spot size), allowing for a mapping of global symmetry. To study how these film properties change with Sn incorporation at a more microscopic level, STEM imaging and spectroscopy were utilized for two characteristic SHG-active samples: one with a low Sn content ($x = 0.09$) and the other with a high Sn content ($x = 0.48$). No evidence of nonstoichiometry-related defects or phases were found for these two samples unlike films without any Sn content ($x = 0$) as discussed earlier. Misfit dislocations were found along the film-substrate interfaces as a result of strain relaxation.

STEM energy dispersive x-ray spectroscopy (EDS) elemental mapping reveals the spatial distribution of Sn and Ti throughout the films as shown in Figs. 3(a) and 3(b) for $x = 0.09$ and 0.48, respectively. Sn enriched regions are observed for both samples but with differences in spatial distribution. At $x = 0.09$, a Sn enriched band up to about 8 nm from the film-substrate interface occurs with about 13% Sn. For the film with the higher Sn content ($x = 0.48$), a similar film thickness was found with the higher Sn content around misfit dislocations near the film-substrate interface. Sn diffusion to the film-substrate interface and defect locations may be a mechanism for strain relaxation and also explains the asymmetry seen in XRD peaks as the lattice parameters in these locations differ from the bulk.

Furthermore, the role of change in the Sn to Ti ratio in determining the polar domain structure is revealed using STEM imaging. The variation in polarization is obtained at the unit cell level using integrated differential phase contrast (iDPC) STEM imaging. The projected polarization (net displacement) for each unit cell is measured as the difference between the cation (Ba^{2+}, Ti^{4+}/Sn^{4+}) and anion (O^{2-}) atom column centers of mass.[32] The polar domain structures are obtained from the compositionally homogeneous regions, above 8 nm from the film-substrate interface as revealed by STEM-EDS in Figs. 3(a) and 3(b). Thin film samples with composition $x = 0.09$ and 0.48 show significant differences in polar structures [Figs. 3(e) and 3(i)]. For the sample with a low Sn content, $x = 0.09$, a long-range polarization can be seen with the majority of the projected polarization oriented out-of-plane, i.e., [001]. Both 90° and 180° domain walls are observed in these films [Fig. 3(e)] as commonly found in BTO.[33] PNRs are also found within the long-range order as marked by enclosed dotted regions in Fig. 3(e). This region consists of a significantly higher polarization along the [0 $\bar{1}$ 0] direction, indicated by light blue, compared to the surrounding area, which has polarization values close to zero, indicated by the darker hues. The existence of such PNRs has been linked to the relaxor ferroelectric behavior, such as in the lead magnesium niobate-lead titanate (PMN-PT) system where a significantly enhanced dielectric and piezoelectric response occurs at the morphotropic phase boundary.[34] In the case of the higher Sn concentration, at $x = 0.48$, a nanoscale domain structure is stabilized as a result of a breakdown of the long-range polarization as shown in Fig. 3(i). The nanoscale polar domain structure resembles the domain pattern of PMN relaxors.[32] However, while no nonstoichiometric inclusions such as BaO are observed, the $x = 0.48$ sample does have other sources of defects such as misfit defects, which can play a role in creating these PNRs. Existence of these nanoscale domains also explains the increase in the width and asymmetry of the (002) film peak and the rocking curve in HRXRD.

The distribution of the projected polar displacements shows directional dependence (out-of-plane along [001] and in-plane along [010]) within a compositionally homogeneous region [Figs. 3(f) and 3(j)]. In the case of a film with a lower Sn content, $x = 0.09$, the mean projected polar displacements along the out-of-plane and in-plane directions are found to be 14 pm and 1 pm, respectively. For the higher Sn content film, $x = 0.48$, the mean out-of-plane displacement decreases to 2 pm, while in-plane shows an increase to 8 pm. The polar plot of displacement vectors

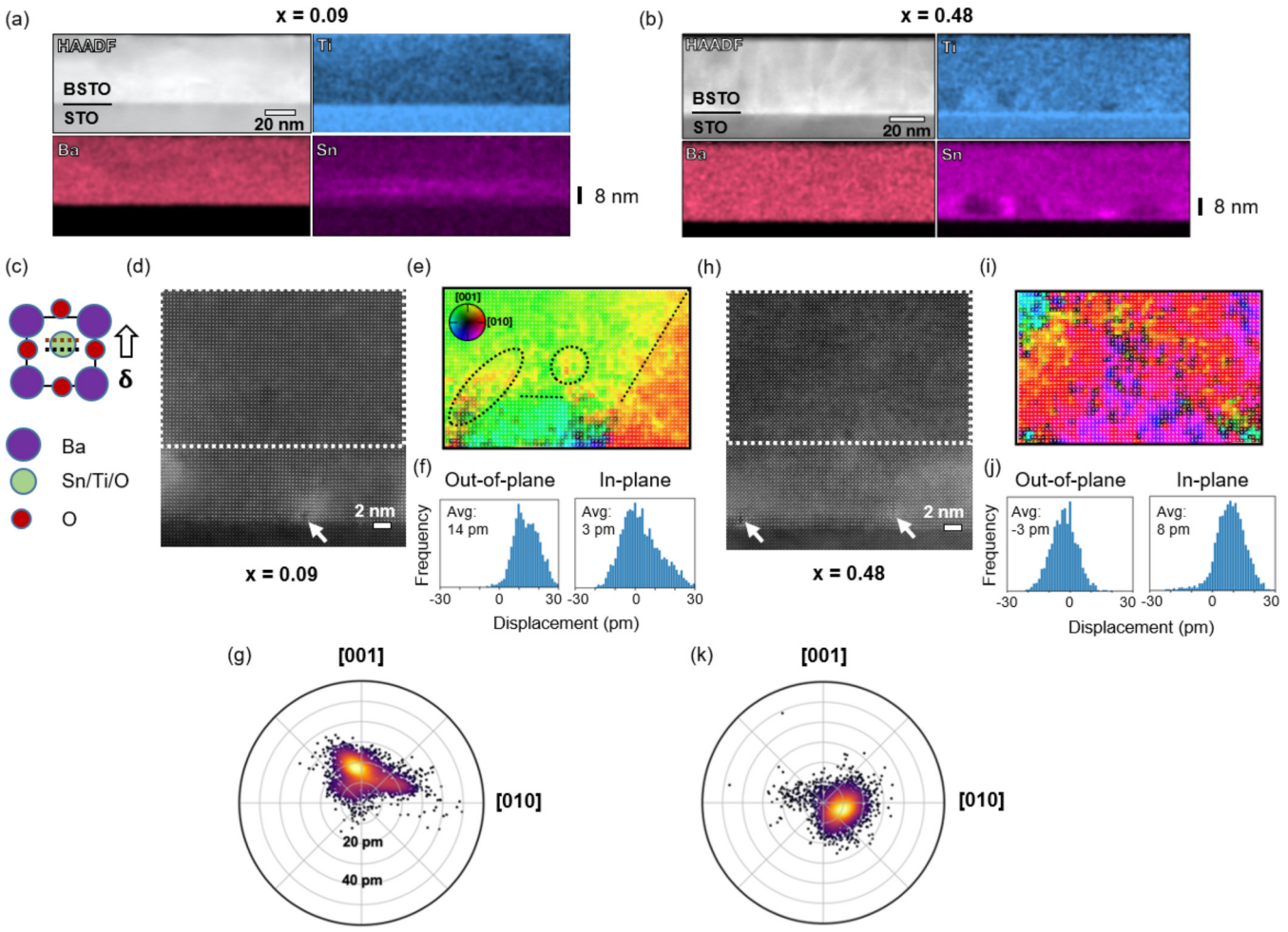

FIG. 3. High-Angle Annular Dark-Field - Scanning Transmission Electron Microscopy (HAADF-STEM) and corresponding EDS maps of Ba, Ti, and Sn for (a) $x = 0.09$ and (b) $x = 0.48$. (c) Schematics showing net displacement (δ) in a unit cell, calculated as the shift in atom column center-of-mass between cations and anions. HAADF-STEM images of the film-substrate interface for (d) $x = 0.09$ and (h) $x = 0.48$. Arrows mark misfit dislocations formed at the film-substrate interface. (e) and (i) are projected displacement (polarization) maps extracted from the highlighted regions away from the film-substrate interface in (d) and (h) for $x = 0.09$ and $x = 0.48$, respectively. The dashed ovals and straight dashed lines indicate PNRs and domain walls, respectively. Histograms of the out-of-plane and in-plane components of the projected displacement are given in (f) for $x = 0.09$ and (j) for $x = 0.48$, respectively. Polar plot of displacement vectors for a thin film sample with composition (g) $x = 0.09$ and (k) $x = 0.48$.

as shown in Figs. 3(g) and 3(k) reveals clear preference of the polar vector toward the out-of-plane direction for $x = 0.09$, in contrast to the in-plane direction with a higher Sn content, $x = 0.48$. This is consistent with polarization measurements from SHG, which show a higher polarization value at $x = 0.09$ along the out-of-plane direction compared to the sample with $x = 0.48$.

III. CONCLUSIONS

In conclusion, BTSO films were grown in the alloy system from $BaTiO_3$ to $BaSnO_3$ using hybrid MBE. Film lattice parameters were found to agree well with Vegard's law and the composition of Sn to Ti could be reliably predicted based solely on the Sn to Ti metal-organic precursor flux ratio. SHG was used to determine overall crystal symmetry and relative polarization. Starting with BSO, a centrosymmetric cubic structure, a transition to a tetragonal structure occurred as Sn was decreased. This trend was also accompanied by an increase in polarization, as estimated by the SHG collected intensity, with a maximum at $x = 0.09$. Finally, from the STEM results, long-range polarization was confirmed in the $x = 0.09$ sample with an out-of-plane cation to anion displacement six times higher than that of $x = 0.48$, the sample which showed the most structural disorder. Inhomogeneities such as clustered octahedral tilt order were found to create polarization barriers and, therefore, led to nanoscale domains in samples with larger Sn compositions. Taken together, these results show $BaTiO_3$–$BaSnO_3$ as a potential system for future lead-free ferroelectrics.

ACKNOWLEDGMENTS

Hybrid MBE growth and characterization of $BaTi_{1-x}Sn_xO_3$ films were supported primarily by the U.S. Department of Energy (DOE) through Grant No. DE-SC0020211. Part of the work was supported as part of the Center for Programmable Energy Catalysis, an Energy Frontier Research Center funded by the U.S. Department of Energy, Office of Science, Basic Energy Sciences at the University of Minnesota, under Award No. DE-SC0023464. Parts of this work were carried out at the Characterization Facility, University of Minnesota, which receives partial support from the NSF through the MRSEC program under Award No. DMR-2011401. This work also benefitted from the Vannevar Bush Faculty Fellowship. Part of this work was carried out at the Minnesota Nano Center, which is supported by the NSF through the National Nano Coordinated Infrastructure under Award No. ECCS-2025124. A.K. and J.M.L. were supported by the Army Research Laboratory via the Collaborative for Hierarchical Agile and Responsive Materials (CHARM) under Cooperative Agreement No. W911NF-19-2-0119. R.Z. and V.G. were supported by the Department of Energy (DOE), Office of Science, Basic Energy Sciences, under Award No. DE-SC002111. B.N. was supported by NSF Research Experiences for Undergraduates (REU) (No. DMR 185-1987). S.Y. and V.G. were supported under Award No. DE-SC0012375.

AUTHOR DECLARATIONS

Conflict of Interest

The authors have no conflicts of interest to disclose.

Author Contributions

William Nunn: Conceptualization (equal); Data curation (equal); Formal analysis (equal); Investigation (equal); Writing – original draft (equal). **Abinash Kumar:** Data curation (equal); Formal analysis (equal); Writing – review & editing (equal). **Rui Zu:** Data curation (equal); Formal analysis (equal); Writing – review & editing (equal). **Bailey Nebgen:** Data curation (equal); Formal analysis (equal); Writing – review & editing (equal). **Shukai Yu:** Data curation (equal); Formal analysis (equal); Writing – review & editing (equal). **Anusha Kamath Manjeshwar:** Data curation (equal); Writing – review & editing (equal). **Venkatraman Gopalan:** Data curation (equal); Funding acquisition (equal); Investigation (equal); Supervision (equal); Writing – review & editing (equal). **James M. LeBeau:** Data curation (equal); Formal analysis (equal); Funding acquisition (equal); Supervision (equal); Writing – review & editing (equal). **Richard D. James:** Conceptualization (equal); Funding acquisition (equal); Supervision (equal); Writing – review & editing (equal). **Bharat Jalan:** Conceptualization (equal); Funding acquisition (equal); Investigation (equal); Project administration (equal); Supervision (equal); Writing – review & editing (equal).

DATA AVAILABILITY

The data that support the findings of this study are available within the article and its supplementary material.

REFERENCES

[1]J. F. Scott, Science **315**, 954 (2007).
[2]G. H. Haertling, J. Am. Ceram. Soc. **82**, 797 (1999).
[3]K. Uchino, *Ferroelectric Devices* (CRC, Boca Raton, FL, 2018).
[4]B. Jaffe, R. S. Roth, and S. Marzullo, J. Appl. Phys. **25**, 809 (1954).
[5]Y. Saito, H. Takao, T. Tani, T. Nonoyama, K. Takatori, T. Homma, T. Nagaya, and M. Nakamura, Nature **432**, 84 (2004).
[6]C.-H. Hong, H.-P. Kim, B.-Y. Choi, H.-S. Han, J. S. Son, C. W. Ahn, and W. Jo, J. Materiomics **2**, 1 (2016).
[7]J. Rödel, W. Jo, K. T. P. Seifert, E.-M. Anton, T. Granzow, and D. Damjanovic, J. Am. Ceram. Soc. **92**, 1153 (2009).
[8]B. N. Rao and R. Ranjan, Phys. Rev. B **86**, 134103 (2012).
[9]S.-T. Zhang, A. B. Kounga, E. Aulbach, H. Ehrenberg, and J. Rödel, Appl. Phys. Lett. **91**, 112906 (2007).
[10]W. Liu and X. Ren, Phys. Rev. Lett. **103**, 257602 (2009).
[11]R. Garg, B. N. Rao, A. Senyshyn, P. S. R. Krishna, and R. Ranjan, Phys. Rev. B **88**, 014103 (2013).
[12]W. Jo, T. Granzow, E. Aulbach, J. Rödel, and D. Damjanovic, J. Appl. Phys. **105**, 094102 (2009).
[13]G. Catalan and J. F. Scott, Adv. Mater. **21**, 2463 (2009).
[14]Y. Yao, C. Zhou, D. Lv, D. Wang, H. Wu, Y. Yang, and X. Ren, Europhys. Lett. **98**, 27008 (2012).
[15]A. K. Kalyani, K. Brajesh, A. Senyshyn, and R. Ranjan, Appl. Phys. Lett. **104**, 252906 (2014).
[16]A. K. Kalyani, H. Krishnan, A. Sen, A. Senyshyn, and R. Ranjan, Phys. Rev. B **91**, 024101 (2015).
[17]S. N. Song, J. W. Zhai, L. N. Gao, X. Yao, T. F. Hung, and Z. K. Xu, J. Appl. Phys. **104**, 096107 (2008).
[18]M. Mascot, D. Fasquelle, and J.-C. Carru, Funct. Mater. Lett. **4**, 49 (2011).
[19]H.-H. Huang, M.-C. Wang, C.-Y. Chen, N.-C. Wu, and H.-J. Lin, J. Eur. Ceram. **26**, 3211 (2006).
[20]H. Cheng, H. Hida, J. Ouyang, and I. Kanno, Ceram. Int. **43**, 1597 (2017).
[21]A. V. Tumarkin, V. M. Stozharov, A. G. Altynnikov, A. G. Gagarin, S. V. Razumov, E. Y. Kaptelov, S. V. Senkevich, I. P. Pronin, and A. B. Kozyrev, Integr. Ferroelectr. **173**, 140 (2016).
[22]G. S. Zhu, D. L. Yan, H. R. Xu, and A. B. Yu, Mater. Lett. **140**, 155 (2015).
[23]Q. Gao, K. Li, K. Zhang, J. Zhang, and Q. Liu, Appl. Phys. Lett. **114**, 081901 (2019).
[24]S. J. Wang, M. O. Lai, and L. Lu, J. Phys. D: Appl. Phys. **43**, 305401 (2010).
[25]Y. Matsubara, K. S. Takahashi, Y. Tokura, and M. Kawasaki, Appl. Phys. Express **7**, 125502 (2014).
[26]W. Nunn *et al.*, J. Vac. Sci. Technol. A **39**, 040404 (2021).
[27]A. Prakash, J. Dewey, H. Yun, J. S. Jeong, K. A. Mkhoyan, and B. Jalan, J. Vac. Sci. Technol. A **33**, 060608 (2015).
[28]O. F. Shoron, S. Raghavan, C. R. Freeze, and S. Stemmer, Appl. Phys. Lett. **110**, 232902 (2017).
[29]D. Lee, F. Liu, T. K. Truttmann, S. A. Chambers, and B. Jalan, Appl. Phys. Lett. **120**, 121604 (2022).
[30]A. R. Denton and N. W. Ashcroft, Phys. Rev. A **43**, 3161 (1991).
[31]S. A. Denev, T. T. A. Lummen, E. Barnes, A. Kumar, and V. Gopalan, J. Am. Ceram. Soc. **94**, 2699 (2011).
[32]A. Kumar, J. N. Baker, P. C. Bowes, M. J. Cabral, S. Zhang, E. C. Dickey, D. L. Irving, and J. M. LeBeau, Nat. Mater. **20**, 62 (2021).
[33]W. J. Merz, Phys. Rev. **95**, 690 (1954).
[34]M. J. Krogstad *et al.*, Nat. Mater. **17**, 718 (2018).
[35]See supplementary material at https://www.scitation.org/doi/suppl/10.1116/6.0002208 for the description of the SHG fitting and for the STEM image of a $BaTiO_3$ film.